



# The application of multidimensional wavelets to unveiling multi-phase diagrams and in situ physical properties of rocks

Oleg V. Vasilyev<sup>a,\*</sup>, Taras V. Gerya<sup>b,c</sup>, David A. Yuen<sup>d</sup>

<sup>a</sup>Department of Mechanical Engineering, University of Colorado, 427 UCB, Boulder, CO 80309, USA

<sup>b</sup>Institut für Geologie, Mineralogie und Geophysik, Ruhr-Universität Bochum, 44780 Bochum, Germany

<sup>c</sup>Institute of Experimental Mineralogy Russian Academy of Sciences, 142432 Chernogolovka, Moscow, Russia

<sup>d</sup>University of Minnesota Supercomputing Institute and Department of Geology and Geophysics, University of Minnesota, Minneapolis, MN 55455-0219, USA

Received 17 November 2003; received in revised form 3 April 2004; accepted 9 April 2004

## Abstract

Calculation of phase diagrams for terrestrial and planetary materials exerts a growing impact in geosciences today. In this work, we demonstrate the feasibility of efficient delineation and visualization of complicated realistic multi-phase diagrams and related in situ physical properties of rocks by using discontinuous second generation wavelets, allowing a representation of both isotropic and anisotropic properties with arbitrary resolution. This is done by combining adaptive wavelet-based meshing technology with recently developed efficient “phase diagram function” designed as a Gibbs free energy minimization. The proposed automated strategy allows one to obtain an efficient delineation of physical properties using a uniform set of wavelet nodes regardless of whether these variables are continuous or discontinuous functions of pressure, temperature, or composition. The use of this strategy captures very small details of phase diagram morphology allowing both acceleration of the calculations and compression of results on the order of  $10^2$  by comparison to uniform grids of the same effective resolution. The web-based application of the proposed methodology for phase diagram visualization with interactive zooming capabilities is also discussed.

© 2004 Published by Elsevier B.V.

*Keywords:* phase diagrams; visualization; automated strategy; discontinuous wavelet transform; wavelet interpolation

## 1. Introduction

Recognition of the important role of phase transformations for the evolution of complex geophysical phenomena has a growing impact for modern geoscience, e.g., [1–4]. Most of these applications are

limited by semi-quantitative analysis of relatively simple systems with few phase transformations [1,3–8]. However, recent development of both large internally consistent, geologically oriented thermodynamic databases [9–12], and state-of-the-art Gibbs energy minimization approach [9,13,14] allow calculation of equilibrium phase assemblages and prediction of in situ physical properties of rocks [15–17]. New challenges emerge when accounting for realistic systems with more than 10 components and complicated non-ideal solid solutions closely representing a variety of

\* Corresponding author.

*E-mail addresses:* [Oleg.Vasilyev@colorado.edu](mailto:Oleg.Vasilyev@colorado.edu)  
(O.V. Vasilyev), [Taras.Gerya@ruhr-uni-bochum.de](mailto:Taras.Gerya@ruhr-uni-bochum.de) (T.V. Gerya),  
[DaveY@krissy.geo.umn.edu](mailto:DaveY@krissy.geo.umn.edu) (D.A. Yuen).

natural terrestrial and planetary materials. Despite the fact that a number of examples of combinations of numerical thermomechanical modeling and Gibbs free energy minimization approaches are present in the literature [17,18], no uniform automated strategy of compact delineation and visualization of complicated realistic phase diagrams and related in situ physical properties of multicomponent systems by geometric mapping methods has been developed up to now.

Calculation and visualization of phase diagrams is computationally intensive. A comprehensive overview of four basic existing computational strategies is given by Connolly and Pettrini [19]. In most automated cases the phase diagrams are calculated either on an a priori distributed dense set of points in phase assemblage space [15–17] or using bisection algorithms [14,20]. The former approach is very expensive and impractical for phase diagrams with dimensions higher than three. The latter lacks the robustness and often requires manual tuning. Robust fully adaptive multi-resolution algorithms for calculation of phase diagrams have not yet been explored.

Alternatively, wavelet-based refining grid strategy can be used to rapidly construct and interrogate multi-phase diagrams. This strategy, originally developed for the solution of elliptic partial differential equations [21], allows automatic grid refinement in the neighborhood of a phase transition. The calculations start on a coarse grid in phase assemblage space. Additional grid points are progressively added with increasing resolution in the regions dictated by the phase diagram. With this adaptive procedure, the grid automatically adjusts to the structure of the phase diagram and results in a minimal number of points in phase assemblage space where calculation of “phase diagram function” is required.

The present paper aims to demonstrate that efficient delineation and visualization of complicated, realistic, multi-phase diagrams and related in situ physical properties of rocks can be reached by using discontinuous second generation wavelets allowing representation of both isotropic and anisotropic properties with arbitrary resolution. This is done by combining adaptive wavelet-based meshing technology [22,23] with recently developed efficient phase diagram function designed as Gibbs free energy minimization procedure [16]. The latter allows the calculation of both the equilibrium phase assemblage

and the corresponding in situ physical properties (density, heat capacity, thermal expansivity, compressibility, etc.) of geological materials of variable chemical composition.

The rest of this paper is organized as follows. Section 2.1 describes the methodology behind calculation of phase diagrams. Section 2.2 describes the discontinuous interpolating wavelet transform that is used for grid adaptation and construction of phase diagrams. The adaptive wavelet-based grid refinement strategy is described in Section 2.3. Section 3 provides salient examples of phase diagram construction using the proposed methodology. Application of the proposed methodology to numerical modeling of geodynamic processes is discussed there as well. Possible extensions of this work, including the interactive web-based applications, are discussed in Section 4.

## 2. Methodology

### 2.1. Phase diagrams

We have employed the Gibbs free energy minimization procedure for determining the equilibrium assemblages and compositions of coexisting phases for a given pressure, temperature and bulk chemical composition of the system. The density was calculated as the ratio of the sum of the molar masses to the sum of the molar volumes of the constituent phases, where each mass and volume is weighted by the mole abundance of the mineral in the rock. The enthalpy was calculated as the ratio of the sum of the molar enthalpies to the sum of the molar masses of the constituent phases, where each mass and enthalpy is weighted by the mole abundance of the mineral in the rock. We have employed a recently developed Gibbs free energy minimization code DEKAP [16] based on the modified version of the algorithm suggested by de Capitani and Brown [14] for complex systems containing non-ideal solid solutions. Thermodynamic data for solid phases and aqueous fluid were taken from the internally consistent database of Holland and Powell [11,12]. Mixing models of solid solutions consistent with this database were taken from the literature [12,24,25].

The system was considered to be open for H<sub>2</sub>O, i.e., the volatiles produced in dehydration reactions

are assumed to be removed. Therefore, although fluid phase saturation was ensured for all calculated equilibrium phase assemblages, such fluids were not involved in density/enthalpy calculations.  $P$ – $T$ -dependent volumes ( $V$ ) and enthalpies ( $H$ ) of phases in equilibrium phase assemblages were calculated via the Gibbs potential,  $G$ , using the respective thermodynamic relations  $V = \partial G / \partial P$  and  $H = G + T \partial G / \partial T$  and a numerical differentiation procedure. In order to simulate melt-absent conditions, a lowered water activity was assumed at temperatures above 630 °C [16]. Thus, we have not considered any melting processes involving the liquidus phase. However, the methodology of minimization allows incorporation of melts into the calculations, when accurate thermodynamic properties of melt components, e.g., [26,27] consistent with database for solid phases, are available.

To provide unique coding of calculated phase assemblages by our “phase diagram function,” we use an output array with dimension equal to the number of chemical components (oxides) in the system. Every phase of thermodynamic database is assigned by a unique index (1, 2, 3, ...). The indexes of phases in equilibrium, calculated for given pressure, temperature and rock composition, are placed in the output array in the increasing order. In case when the number of calculated equilibrium phases is less than the number of chemical components last positions of the output array are filled by 0 index. Thus, every unique phase assemblage has a unique combination of phase indexes placed in the output array. This combination is then processed by the wavelet program providing comparison of the newly coming phase assemblage with previously found unique phase assemblages. Overall numbering of the unique assemblages is done by the wavelet program. In order to increase visual contrast between the unique phase assemblages, these assemblages are randomly reshuffled.

## 2.2. Discontinuous interpolating wavelet transform

Interpolating wavelets [28,29] are best suited to represent continuous changes in the field variables. In the case of phase diagrams, the continuity requirement is obviously not satisfied insofar as both phase assemblages and calculated physical properties

may exert discontinuous (step-like) changes across phase boundaries, e.g., [16,17]. To resolve this problem we developed the discontinuous interpolating wavelet transform. Discontinuous interpolating wavelets are the generalization of the interpolating wavelets of Donoho [28] and Harten [29] and second-generation wavelets [30,31]. This section briefly describes the construction of the discontinuous interpolating wavelet transform. To the best of our knowledge, this is the first time the discontinuous wavelet transform is introduced. For readers who are interested in coding discontinuous interpolating wavelet transform themselves, a schematic algorithm is provided in Appendix A.

The algorithm for constructing discontinuous interpolating wavelets on an interval is basically the same as in [32] with the exception that a polynomial interpolation is not allowed across the phase boundaries, which are assumed to be known a priori. The main difference is in construction of local interpolating polynomials,  $P_p(x)$  (see Appendix A.1) that use  $2N$  closest points that belong to the same phase assemblage. If for a given resolution, the number of closest points belonging to the same phase assemblage is less than  $2N$ , the order of the polynomial drops accordingly. However, for the finer levels of the resolution the polynomial order would increase back to  $p = 2N - 1$ .

To illustrate how discontinuous interpolating wavelet transform improves the results when applied to discontinuous fields, we consider a function that is discontinuous at the interface (see Fig. 1a). Two distinct phase assemblages are shown in Fig. 1b. The function is sampled on a very coarse grid ( $17 \times 17$ ) and then both continuous and discontinuous wavelet transforms are performed on this grid. After that the wavelet interpolation to  $257 \times 257$  grid is performed via the inverse wavelet transform. The results of a standard (continuous) and discontinuous wavelet interpolations are shown in Fig. 1c and d, respectively. As easily seen, the discontinuous wavelet transform drastically improves the results, which is mostly due to the fact that no interpolation is done across the phase boundaries. This property together with adaptive capabilities, which are discussed next, make discontinuous wavelet transform a very useful tool for phase diagram construction.

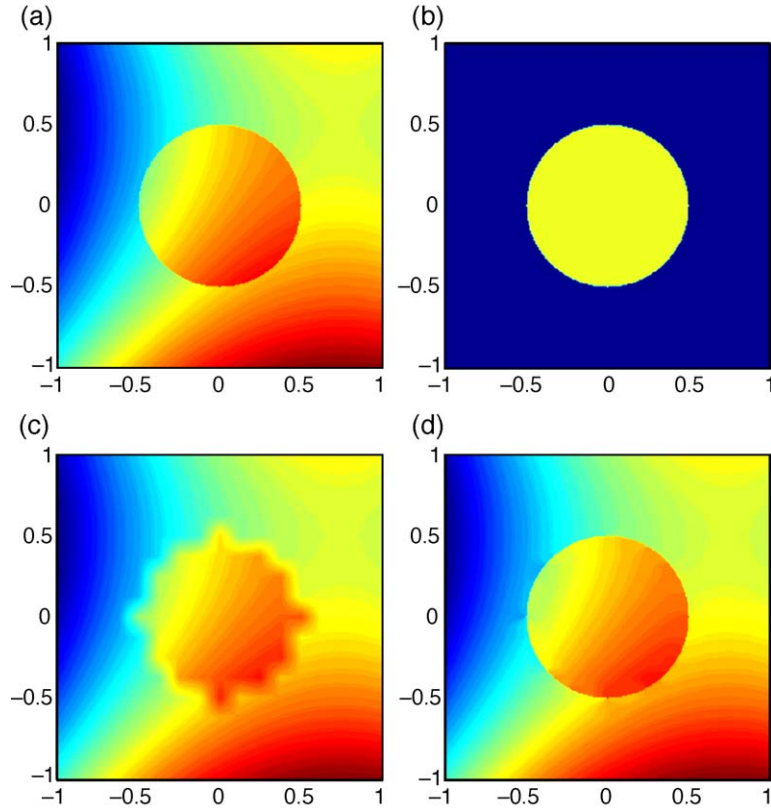


Fig. 1. Example of wavelet interpolation of a function sampled on  $17 \times 17$  to  $257 \times 257$  grid: (a) original function, discontinuous at the interface, (b) phase assemblages, (c) standard wavelet interpolation, (d) discontinuous wavelet interpolation.

### 2.3. Adaptive wavelet based refinement

A wavelet-based refining grid strategy is ideally suited for construction of phase diagrams. This strategy, originally developed for the solution of elliptic partial differential equations [34], allows automatic grid refinement in the neighborhood of phase transitions. Grid adaptation occurs naturally in wavelet methods and is based on the analysis of wavelet coefficients. As shown in Appendix A.2, a function  $f(\mathbf{x})$  can be decomposed as

$$f(\mathbf{x}) = \sum_{\mathbf{k} \in \mathbf{K}^0} c_{\mathbf{k}}^0 \phi_{\mathbf{k}}^0(\mathbf{x}) + \sum_{j=0}^{+\infty} \sum_{\mu=1}^{2^n-1} \sum_{\mathbf{l} \in \mathcal{L}^{\mu,j}} d_{\mathbf{l}}^{\mu,j} \psi_{\mathbf{l}}^{\mu,j}(\mathbf{x}). \quad (1)$$

The strength of the wavelet approach now appears. For functions which contain isolated small scales on a

large-scale background, most wavelet coefficients are small, thus a good approximation is retained even after discarding a large number of wavelets with small coefficients. Intuitively, the coefficient  $d_{\mathbf{l}}^{\mu,j}$  will be small unless  $f(\mathbf{x})$  varies on the scale of  $j$  in the immediate vicinity of wavelet  $\psi_{\mathbf{l}}^{\mu,j}(\mathbf{x})$ . In fact, the error incurred by ignoring coefficients with magnitude lower than  $\epsilon$  is  $O(\epsilon)$ . More precisely, if we rewrite Eq. (1) as a sum of two terms composed respectively of wavelets whose amplitude is above and below some prescribed threshold  $\epsilon$ , i.e.,  $f(\mathbf{x}) = f^{\geq}(\mathbf{x}) + f^{<}(\mathbf{x})$ , then it can be shown [22,35] that

$$f(\mathbf{x}) - f^{\geq}(\mathbf{x}) \leq C_1 \epsilon \leq C_2 \mathcal{N}^{-p/n}, \quad (2)$$

where  $\mathcal{N}$  is the number of significant wavelet coefficients,  $p = 2N - 1$  is the order of the wavelets, and  $n$  is the dimensionality of the problem.

In order to realize the benefits of the wavelet compression, we need to be able to reconstruct  $f \geq (\mathbf{x})$  from the subset of  $\mathcal{N}$  grid points, denoted by  $\mathcal{G}_\geq$ . Note that every wavelet  $\psi^{ij}(\mathbf{x})$  is uniquely associated with a collocation point. Consequently, the collocation point should be omitted from the computational grid if the associated wavelet is omitted from the approximation. The details of grid adaptation procedure are given in Appendix A.3. With this adaptive procedure the grid automatically adjusts to the structure of the phase diagram and results in a minimal number of points in phase assemblage space, where calculation of “phase diagram function” is required.

### 3. Results and discussion

Figs. 2–4 show the results of calculation of the phase diagram and the related physical properties for the bulk chemical composition of typical high-grade metapelite [33]. Examples of phase assemblages and compositions of coexisting phases for this metapelite and other common rock types calculated with DEKAP program are presented in [16]. Initial wavelet grid (Fig. 2a) is taken to be uniform ( $33 \times 33$  nodes) and only partly and very roughly represent phase transitions (Fig. 2b) and distribution of density (Fig. 2c) and enthalpy (Fig. 2d) in  $P$ – $T$  space. On the other hand, the final distribution of wavelet nodes in  $P$ – $T$  diagram

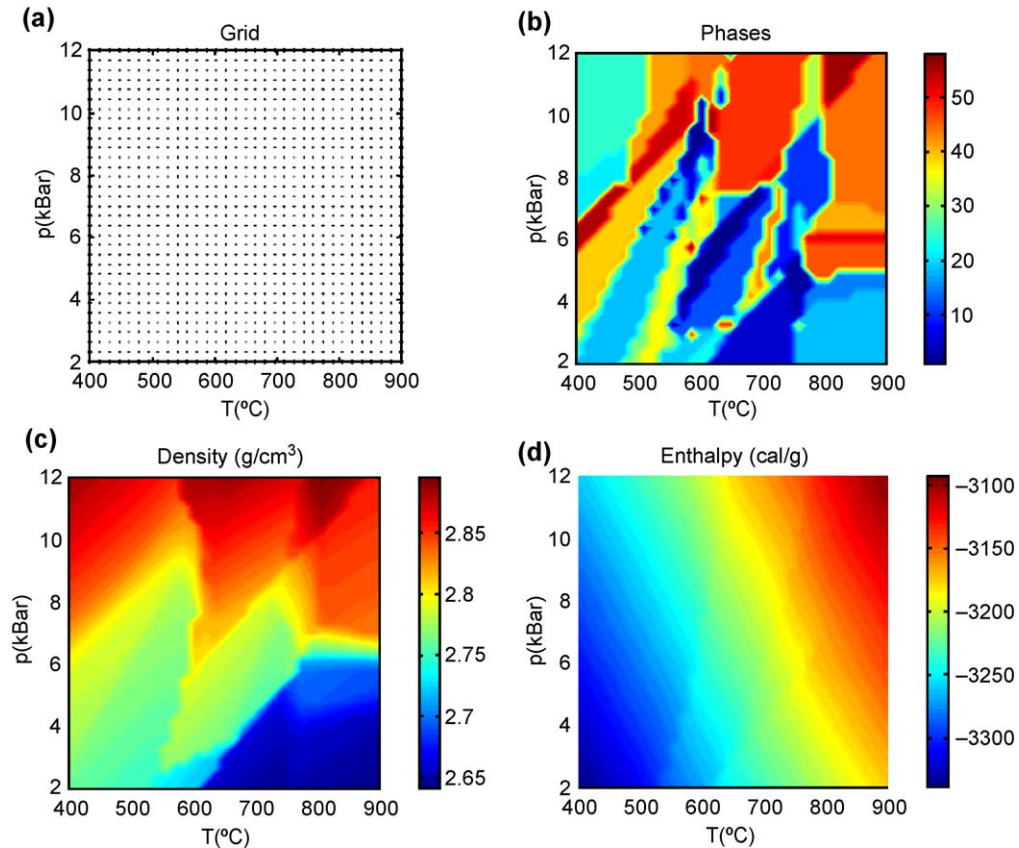


Fig. 2. Initial distribution of wavelet nodes (a) and corresponding phase diagram (b) compared to density (c) and enthalpy (d) maps in  $P$ – $T$  coordinates. Diagrams are calculated for the composition of typical high-grade metapelite [33] within 2–12 kbar pressure range and 400–900  $^{\circ}\text{C}$  temperature range. Fifty-seven different colors in panel (b) correspond to 57 different phase assemblages (see Fig. 4 for examples of these assemblages) found for the given distribution of wavelet nodes. Lowered water activity at high temperature was used to ensure melt-free conditions [16].

after 8 cycles of adjusting (Fig. 3a) is highly inhomogeneous following boundaries of different phase assemblages (Fig. 3b) and related sharp changes in calculated physical properties (cf. Fig. 3b and c). The strategy of calculation includes both refinement and coarsening of initial  $33 \times 33$  regular grid in different areas of  $P$ – $T$  diagram depending on distribution of approximating phase assemblages and physical properties in  $P$ – $T$  space. The proposed automated strategy allows efficient delineation of physical properties with contrasting distributions, using a uniform set of wavelet nodes: compare the sharp variations in mineral assemblages (Fig. 3b) with the continuous–discontinuous distribution of density (Fig. 3c) and relatively smooth changes in enthalpy (Fig. 3d). The use of this strategy captures the very minute details of the phase

diagram morphology, and also allows zooming in of the most complicated regions (Fig. 4). This strategy allows both acceleration of the calculations and compression of the results on the order of  $10^2$  by comparison to uniform grids with the same effective resolution.

### 3.1. Application to numerical thermomechanical modeling

One of the straightforward application of developed approach is the use of calculated phase diagrams and related in situ transport properties for numerical modeling of geodynamic processes. Account for thermal and density effects of phase transformations including melting processes pose significant chal-

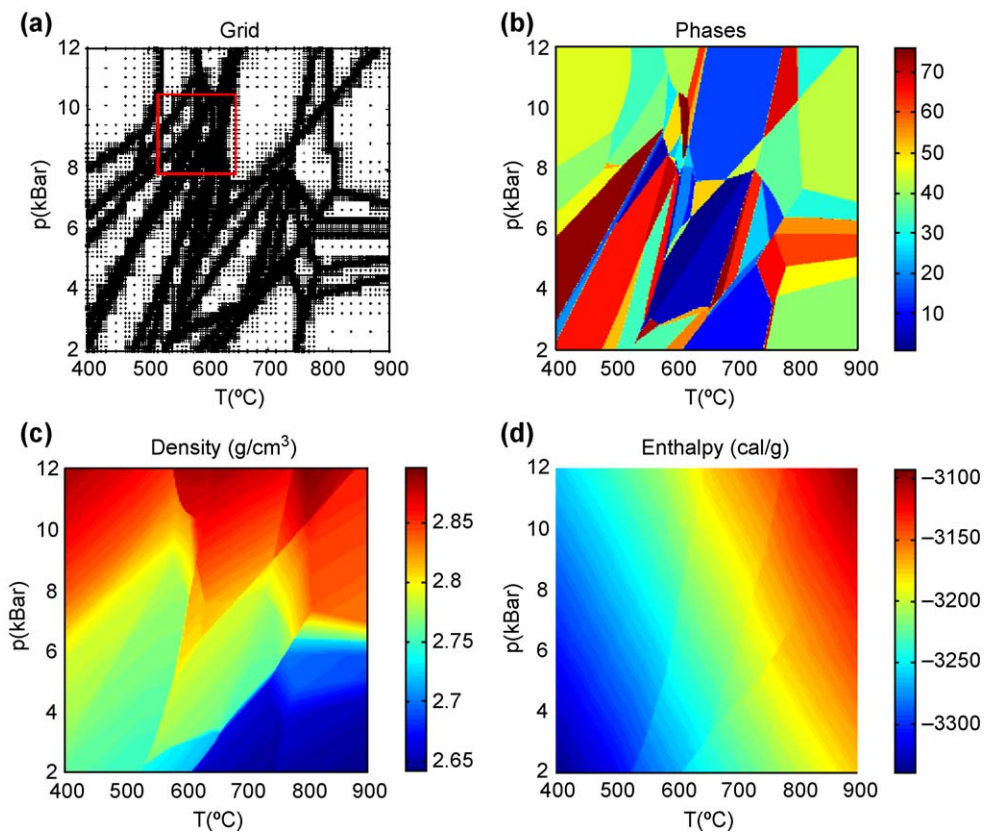


Fig. 3. Final distribution of wavelet nodes (a) and corresponding phase diagram (b) compared to density (c) and enthalpy (d) maps in  $P$ – $T$  coordinates. Parameters for calculation are the same as for Fig. 2. Seventy-five different colors in panel (b) correspond to 75 different phase assemblages (see Fig. 4 for examples of these assemblages) found for the given distribution of wavelet nodes. Red square in panel (a) shows area amplified in Fig. 4.

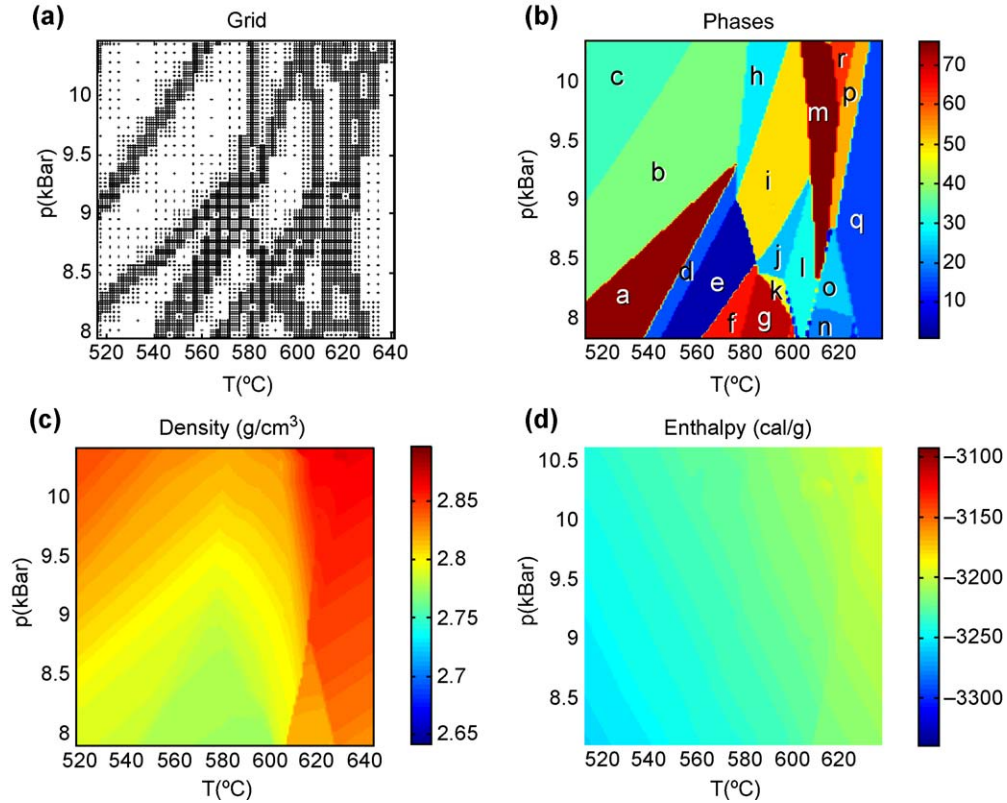


Fig. 4. Zoomed area of the diagrams shown in Fig. 3. Fine details of different phase assemblages (b) are captured by adjusted wavelet distribution (a). Corresponding density (c) and enthalpy (d) distribution is clearly seen. Letters in (b) denote different phase assemblages (+Q+Ru+Mu+Mt): a → Pa+Chl+Ep+Pl, b → Pa+Chl+Ep+Pl+Grt, c → Pa+Chl+Ep+Pl+Grt+Bt, d → Pa+Chl+Ep+Pl+fluid, e → Pa+Chl+Pl+fluid, f → Chl+Pl+fluid, g → Chl+Pl+Ilm+fluid, h → Pa+Chl+Ep+Pl+Grt+fluid, i → Pa+Chl+Pl+Grt+fluid, j → Chl+Pl+Grt+fluid, k → Chl+Pl+Grt+Ilm+fluid, l → Chl+Pl+Grt+Bt+fluid, m → Pa+Chl+Pl+Grt+Bt+fluid, n → Pl+Bt+St+fluid, o → Pl+Grt+Bt+St+fluid, p → Pa+Pl+Grt+Bt+Ky+fluid, q → Pl+Grt+Bt+Ky+fluid, r → Pa+Pl+Grt+Bt+fluid, where Chl, Pl, Grt, St, Ep, Bt, Mu are solid solutions. Mineral abbreviations are taken from [12].

lenges for thermomechanical modeling, e.g., [6,36,39–41]. As shown by Barboza and Bergantz [39] abrupt changes in phase state associated with the disappearance of a phase to be difficult to accommodate in a numerical model especially to the continuity condition. To overcome these difficulties we used the simplified approach combining incompressible fluid approximation for the continuity equation and numerical smoothing of thermal and density effects of phase transformations for momentum and temperature equation [36]. According to our numerical approach based on finite differences and marker in cell technique [37,38] transport properties are computed for many markers displaced by velocity field. Effective density ( $\rho$ ), isobaric heat capacity ( $C_p$ ), and thermal expansion

( $\alpha$ ) of each marker are calculated via equilibrium enthalpy and density described in wide  $P$ – $T$  interval for every particular rock composition (e.g., Fig. 4). Effective density is calculated for each marker as an average value within  $10 \text{ K} \times 200 \text{ bar}$  intervals around actual values of  $P$  and  $T$  for this marker. Effective isobaric heat capacity and thermal expansion are calculated via enthalpy and density, according to the following standard thermodynamic relations:

$$C_p = \left( \frac{\partial H}{\partial T} \right)_P$$

$$\alpha = \frac{\rho}{T} \left[ \frac{1}{\rho} - \left( \frac{\partial H}{\partial P} \right)_T \right].$$

We use numerical differentiation procedure with 10 K and 200 bar step for  $T$  and  $P$ , respectively, to avoid abrupt changes in effective  $C_p$  and  $\alpha$  values. We also used a time-step limitation to ensure less than 10 °C changes in temperature for each computation step. Fig. 5 shows an example of thermo-mechanical modeling of crustal convection in collisional orogen accounting for thermal and density effects of phase transformations. As shown in our recent study [36], crustal convection enhanced by density effects of phase transformations (Fig. 5c) is very efficient at elevated temperatures (Fig. 5a) providing rapid exhumation of lower crustal rock toward the surface (Fig. 5b). This study show

potential importance of automated coupling between numerical modeling and phase diagram calculations. Further methodological challenges in this direction are related to correct solving of continuity condition, e.g., [39], and accounting for kinetics of phase transformations.

#### 4. Conclusion and perspectives

This paper is restricted to a relatively simple, two-dimensional thermodynamic system with only a few interpolated variables, namely phase assemblages, density and enthalpy. We have demonstrated

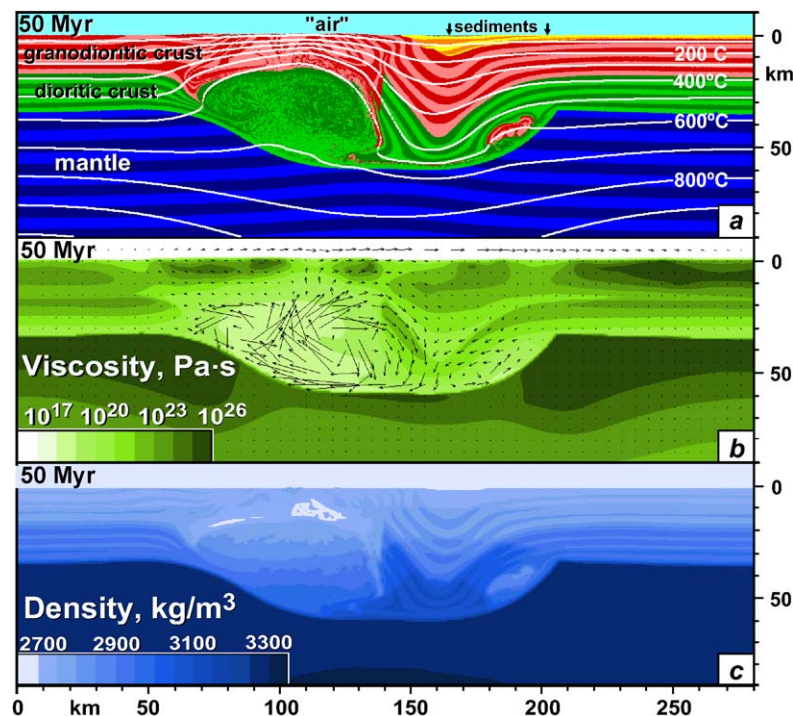


Fig. 5. Example of thermomechanical modeling of crustal convection in collisional orogen coupled with calculations of in situ physical properties of crustal rocks [36]. (a) Distributions of different rock types (color code) and isotherms (white lines). (b) Distribution of effective viscosity (color code) and velocity field (arrows). (c) Distribution of calculated in situ rock density used for thermomechanical calculations. The thermomechanical grid configuration is  $281 \times 101$  regularly spaced points and 700,000 markers are employed. Boundary conditions: top—free sleep,  $T=25$  °C; walls—free sleep, no horizontal heat flow; bottom—“infinity” (permeable boundary with  $\partial P/\partial x=0$ ,  $\partial v_x/\partial z=0$  and  $\partial^2 T/\partial z^2=0$ , where  $x$  and  $z$  are the horizontal and the vertical coordinates, respectively, and  $v_x$  is the horizontal velocity component). Numerical code I2VIS based on finite differences and marker in cell technique [37,38] is used for thermomechanical modeling. We have not considered phase transformations for the mantle rock. Further details of thermomechanical modeling and phase diagrams for crustal rocks are given in [36].

that wavelet transforms can be employed as a straightforward and easy-to-use tool for delineating the phase boundaries and determining thermodynamic quantities, such as the density and enthalpy in multi-component systems. Further progress is related to the calculation and visualization of phase diagrams and rock physical properties in multidimensional space defined by more than two thermodynamic parameters as pressure, temperature, water fugacity, chemical components, etc. The use of such diagrams for numerical thermomechanical modeling of effects of realistic phase transformations in evolving multi-phase geophysical flows [17] may also be considered as an important direction for future development. The scheme of our method is summarized in Fig. 6, where we sketch the procedure to be followed from the use of free energy down to the construction of the phase boundaries by means of wavelet-transformed quantities and its inverse transformed counterpart. The last step in Fig. 6 emphasizes the importance of using webtools to interrogate the large data sets in terms of a large data base. The ability to zoom into the data and to visualize the complicated phase boundaries is an important aspect of this kind of web-based set up [42].

Apart from multi-dimensional phase diagrams, wavelet-based delineation and visualization strategy can also have broad applications in other geophysical and petrological fields. For example, the discontinuous wavelet transform developed here may be a very useful tool for compact storage and visualization of large ultrahigh-resolution numerical experiments for multi-phase geophysical flows consisting of many different chemical components and characterized by both continuous and discontinuous spatial and temporal variations in multiple field properties, e.g., [41,43]. Delineation, visualization and mathematical, e.g., statistical, processing of phase boundaries in 2D and 3D real-space has multiple applications in modern geosciences often dealing with complicated deformed and partially molten polycrystalline experimental and natural materials [44–46]. This is especially important for microstructural analysis [44] and investigation of rheological properties of various rocks and mineral aggregates [45–49]. As a source of data for automatic processing,

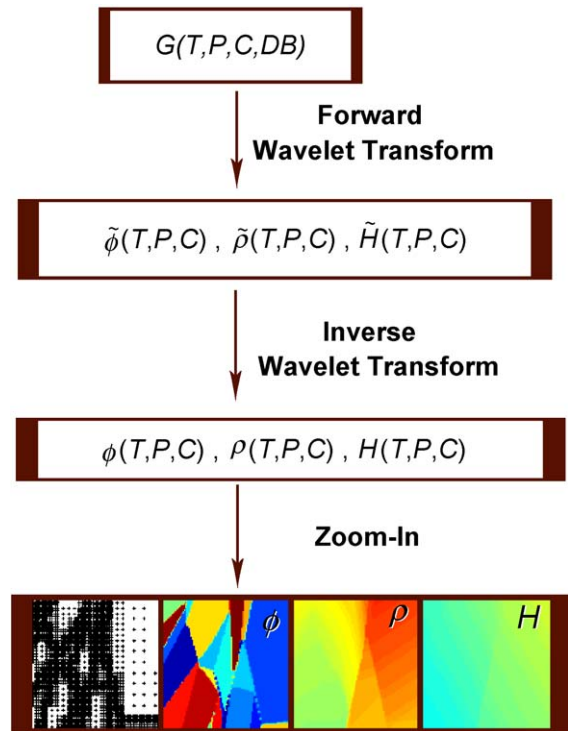


Fig. 6. Schematic diagram showing the determination of phase assemblage and physical properties from the Gibbs free energy  $G$ .  $G$  is the Gibbs free energy of the system in the equilibrium state calculated from classical thermodynamics.  $T$ ,  $P$ ,  $C$  and  $DB$  are the temperature, pressure, chemical composition of the system and internally consistent thermodynamic database used for Gibbs free energy calculation, respectively. The phase assemblages  $\phi$ , density  $\rho$  and enthalpy  $H$  are then wavelet-transformed to obtain an optimized description of the system. Inverse wavelet-transforms bring optimized wavelet-based description back into real quantities in physical space defined by ranges of  $T$ ,  $P$  and  $C$  variations. The details of the phase diagram, density and enthalpy are then zoomed-in by interpolation. This data set can be accessed over the internet by interrogative techniques using the server–client paradigm [42].

high-resolution electronic and optical microscopy images are broadly used. The greatest novelty in this work is the use of high-resolution computed X-ray tomography (HRX-ray CT), a new technique for obtaining digital 3D images of the interiors of polycrystalline objects [50–52]. Taking into account that in the same deformed mineral aggregate grain size commonly vary over several orders of magnitude [44], application of the

wavelet-based delineation, reconstruction and visualization of 2D and 3D phase boundaries will greatly facilitate and strengthen existing post-processing procedures opening new opportunity for further mathematical analysis. In this respect (i) post-processing of the result of rheological experiments in the case of grain size sensitive diffusional creep of solid and partially molten aggregates [45,46,49] and (ii) study of melt dynamics in crust and mantle using data on experimental and natural systems with partially molten both deformed and undeformed rocks [53,54] seem to be obvious important areas for the immediate application of presented adaptive wavelet-based technology.

There are immense computational and visualization challenges arising in higher dimensions as the number of components in the system increase. These include the memory requirements due to the growing dimensionality of the problem, which will grow up exponentially with the increase of the dimensionality. Some clever strategy must be devised to cope with this situation as well as visualization of the multidimensional images using packages such as Amira [55] on shared-memory processors. The same technique can be employed to study rheology in grain-size distributions [56] and melt domains from microscopy [57].

## Acknowledgements

Partial support for the first author (O.V. Vasilyev) was provided by the National Science Foundation under grants No. EAR-0242591, EAR-0327269, and ACI-0242457. The second author (T.V. Gerya) was supported by RFBR grants No. 03-05-64633 and 1645-2003-5, by an Alexander von Humboldt Foundation Research Fellowship, and by the Deutsche Forschungsgemeinschaft within Sonderforschungsbereich 526. The third author (D.A. Yuen) was supported by the National Science Foundation under grants No. EAR-0106276 and EAR-0327387. We are also grateful to J.A.D. Connolly and Yu.Yu. Podladchikov for the discussions that motivated this work. *[SK]*

## Appendix A. Discontinuous interpolating wavelet transform

This appendix briefly describes the essential components of discontinuous wavelet transform, wavelet construction, and adaptive grid refinement. It is mainly written for readers, who is interested in coding discontinuous interpolating wavelet transform themselves. The provided pseudo-codes are detailed enough, so anybody with very little knowledge of wavelet theory is capable of programming the algorithm. For readers, who are interested in mathematical details of the algorithm, we refer to the following papers [22,30–32,58]. As we pointed out earlier, the discontinuous interpolating wavelet transform algorithm only differs in details of polynomial interpolation by not allowing it across the phase boundaries, which will be further elaborated on.

We start by discussing the construction of discontinuous interpolating wavelet transform on an interval. Then extend it to multiple dimension. Finally, details of wavelet transform on adaptive grid and adaptive grid refinement strategies will be discussed.

### A.1. One-dimensional transform

Wavelets can be constructed on an interval to start, an arbitrary (usually uniformly spaced) set of grid points  $x_k$ , ( $k=0, \dots, 2^J m$ ) needs to be defined. With this construction we have  $2^J m + 1$  grid points. The next step is to define the set of nested dyadic grids  $x_k^j$  ( $j=0, \dots, J$ ,  $k=0, \dots, 2^j m$ ), which are formed by a simple restriction rule  $x_k^j = x_{2k}^{j+1}$ ,  $j=0, \dots, J-1$ . Now the meaning of parameters  $J$  and  $m$  is clear.  $J+1$  is the total number of nested levels (levels of resolution), while  $m+1$  is the total number of grid points on the coarsest level. For convenience of the discussion, a collection of grid points belonging to the same level of resolution,  $j$ , will be called grid  $\mathcal{G}^j$ . Example of uniformly spaced dyadic nested grids  $\mathcal{G}^j$  for  $j=0, \dots, 4$  are given in Fig. 7.

Interpolating discontinuous wavelets can be formally introduced through the recursive interpolating subdivision scheme of Deslauriers and Dubuc [59], which considers the problem of building an inter-

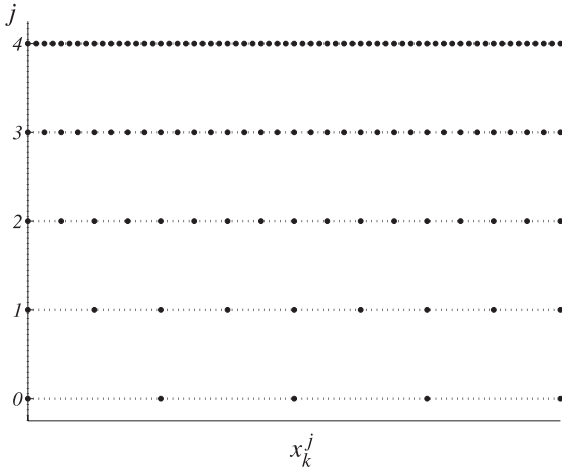


Fig. 7. Example of nested grids on an interval.

polant  $f^j(x)$  on a grid  $\mathcal{G}^{j+1}$  for a given data sequence  $f(x_k^j)$ . The subdivision scheme consists of the recursive procedure of interpolating the data  $f_k^j = f(x_k^j)$  to all dyadic points in between. The algorithm proceeds by interpolating the data  $f(x_k^j)$  to the points on a grid  $\mathcal{G}^{j+1}$ , which do not belong to  $\mathcal{G}^j$ . This procedure does not modify any of the existing data, and thus can be repeated until the data are interpolated to all dyadic points up to the desired level of resolution. The interpolation is achieved by constructing local polynomials,  $P_p(x)$  of order  $p = 2N - 1$ , which uses  $2N$  closest points that belong to the same phase assemblage. If for a given resolution, the number of closest points belonging to the same phase assemblage is less than  $2N$ , the order of the polynomial drops accordingly. However, for the finer levels of the resolution the polynomial order would increase back to  $p = 2N - 1$ . For example, to find the value of the interpolant at location  $x_{2k+1}^{j+1}$  we construct the polynomial of order  $2N - 1$  based on the values of the function at the closest locations  $x_{k+1}^j$  that belong to the same phase assemblage as  $x_{2k+1}^{j+1}$ . Let  $\mathcal{L}_p^j(x_{2k+1}^{j+1})$  denote the set of such points. Note that when there exist  $N$  points on each side of  $x_{2k+1}^{j+1}$  that belong to the same phase assemblage,  $\mathcal{L}_p^j(x_{2k+1}^{j+1}) = -N + 1, \dots, N$ . The simplest way to construct such a polynomial is to use Lagrange interpolation that can be found in any textbook on

numerical methods. Thus, evaluating this polynomial at point  $x_{2k+1}^{j+1}$  and substituting the values of polynomial coefficients expressed in terms of values  $f(x_k^j)$  we can easily get that

$$f^j(x_{2k+1}^{j+1}) = \sum_{l \in \mathcal{L}_p^j(x_{2k+1}^{j+1})} w_{k,l}^j f(x_k^j), \quad (3)$$

where  $w_{k,l}^j$  are the weights of Lagrange interpolating polynomial.

The interpolating scaling function  $\phi_k^j(x)$  can be formally defined by setting  $f(x_k^j) = \delta_{l,k}$ , where  $\delta_{l,k}$  is Kronecker delta, and then performing the interpolating subdivision scheme up to an arbitrary high level of resolution  $J$ . This procedure will result in the scaling function  $\delta_k^j$  sampled at the locations  $x_k^j$ . Now, using the linear superposition, it is easy to show that

$$f^j(x) = \sum_k c_k^j \phi_k^j(x), \quad (4)$$

where for consistency with wavelet notation we set  $c_k^j = f(x_k^j)$ . It is easy to show that for the regularly spaced grid  $\mathcal{G}^j$ , all scaling functions are translates and dilates of one function  $\phi(x) = \phi_0^0(x)$ , called interpolating scaling function. An example of interpolating scaling function  $\phi(x)$  for  $N=3$  is shown in Fig. 8 [28,60].

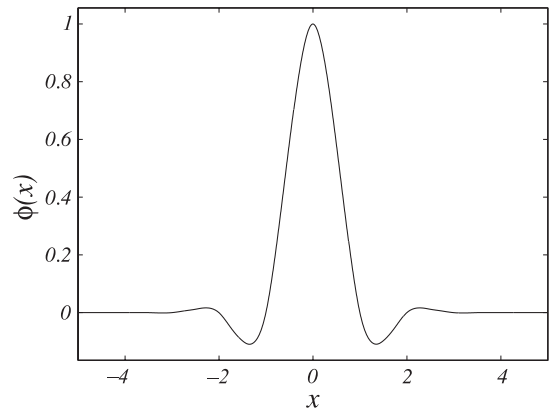


Fig. 8. Interpolating scaling function  $\phi(x)$ .

**Algorithm 1.**

Forward discontinuous interpolating wavelet transform on an interval.

---

```

for all levels  $j = J - 1 : -1 : 0$ 
  do  $k = 0 : 1 : 2^j m - 1$ 
    
$$d_k^j = \frac{1}{2} \left( c_{2k+1}^{j+1} - \sum_{l \in \mathcal{L}_p^j(x_{2k+1}^{j+1})} w_{k,l}^j c_{2k+2l}^{j+1} \right)$$

    
$$c_k^j = c_{2k}^{j+1}$$

  enddo
end

```

---

**Algorithm 2.**

Inverse discontinuous interpolating wavelet transform on an interval.

---

```

for all levels  $j = 0 : 1 : J - 1$ 
  do  $k = 0 : 1 : 2^j m - 1$ 
    
$$c_k^j = c_{2k}^{j+1}$$

    
$$c_{2k+1}^{j+1} = 2d_k^j + \sum_{l \in \mathcal{L}_p^j(x_{2k+1}^{j+1})} w_{k,l}^j c_{2k+2l}^{j+1}$$

  enddo
end

```

---

**Algorithm 3.**

In-place forward discontinuous interpolating wavelet transform on an interval.

---

```

for all levels  $j = J - 1 : -1 : 0$ 
   $s = 2^{J-j-1}$ 
  do  $k = 0 : s : 2^{J-1} m - s$ 
    
$$f_{2k+s} = \frac{1}{2} \left( f_{2k+s} - \sum_{l \in \mathcal{L}_p^j(x_{2k+s}^j)} w_{k,l}^j f_{2k+2sl} \right)$$

  enddo
end

```

---

**Algorithm 4.**

In-place inverse discontinuous interpolating wavelet transform on an interval.

---

```

for all levels  $j = J - 1 : -1 : 0$ 
   $s = 2^{J-j-1}$ 
  do  $k = 0 : s : 2^{J-1} m - s$ 
    
$$f_{2k+s} = 2f_{2k+s} + \sum_{l \in \mathcal{L}_p^j(x_{2k+s}^j)} w_{k,l}^j f_{2k+2sl}$$

  enddo
end

```

---

Repeating the procedure for  $j+1$  level of resolution, we construct the function  $f^{j+1}(x)$ . Due to the properties of interpolating subdivision scheme discussed above, it follows that  $f^{j+1}(x_k^j) = f(x_k^j)$ . However,  $f^j(x_{2k+1}^{j+1}) \neq f^{j+1}(x_{2k+1}^{j+1})$ . Thus, we can define the detail function  $d^j(x)$  to be the difference between  $f^{j+1}(x)$  and  $f^j(x)$ . If we define half the difference  $f^{j+1} - f^j$  at location  $x_{2k+1}^{j+1}$  to be a wavelet coefficient  $d_k^j$ , then it can be easily shown that

$$d^j(x) = \sum_m d_m^j \psi_m^j(x), \quad (5)$$

where  $\psi_k^j(x) = 2\phi_{2k+1}^{j+1}(x)$  is the wavelet function. Using Eqs. (4) and (5), we obtain

$$\sum_k c_k^{j+1} \phi_k^{j+1}(x) = \sum_l c_l^j \phi_l^j(x) + \sum_m d_m^j \psi_m^j(x). \quad (6)$$

Now we are in position to introduce a discontinuous interpolating transform. Starting at the finest level of resolution, we obtain  $c_k^J = f(x_k^J) = f_k$ , wavelet coefficients  $d_k^j$  can be found recursively using the using forward discontinuous wavelet transform given in Algorithm 1. The inverse transform is a simple reversion of the operations and is given in Algorithm 2. The strength of the wavelet transform is that it can be performed in-place, i.e., wavelet coefficients can be stored at the locations of the original function. Once the transform is performed, wavelet coefficients can be recovered from the transformed vector using the fol-

lowing rule  $d_k^j \rightarrow f_{2^{j-1}(2k+1)}$ . With these convention, the forward and inverse wavelet transforms can be rewritten in more practical forms, respectively given in Algorithms 3 and 4.

---

```

for all levels  $j = J - 1 : -1 : 1$ 
   $s = 2^{J-j-1}$ 
  do  $k_y = 0 : s : 2^{J-j} m_y$ 
    do  $k_x = 0 : s : 2^{J-1} m_x - s$ 
       $f_{2k_x+s, k_y} = \frac{1}{2} \left( f_{2k_x+s, k_y} - \sum_{l \in \mathcal{L}_p^j(x_{2k_x+s}, y_{k_y}^j)} w_{k,l}^j f_{2k_x+s, k_y} \right)$ 
    enddo
  enddo
  do  $k_x = 0 : s : 2^{J-j} m_x$ 
    do  $k_y = 0 : s : 2^{J-1} m_y - s$ 
       $f_{k_x, 2k_y+s} = \frac{1}{2} \left( f_{k_x, 2k_y+s} - \sum_{l \in \mathcal{L}_p^j(x_{k_x}^j, y_{2k_y+s}^j)} w_{k,l}^j f_{k_x, 2k_y+s} \right)$ 
    enddo
  
```

---

### Algorithm 5.

In-place forward discontinuous interpolating wavelet transform in two dimensions.

#### A.2. Multi-dimensional transform

Wavelet construction can be easily extended to multiple dimensions using tensor product wavelets, which in two dimensions can be written as

$$\psi_{i,k}^{\mu,j}(\mathbf{x}) = \begin{cases} \psi_i^j(x_1) \phi_k^j(x_2) & \mu = 1 \\ \phi_i^j(x_1) \psi_k^j(x_2) & \mu = 2 \\ \psi_i^j(x_1) \psi_k^j(x_2) & \mu = 3 \end{cases} \quad (7)$$

with a two-dimensional scaling function  $\phi_{i,k}^j(\mathbf{x}) = \phi_i^j(x_1) \phi_k^j(x_2)$ , where  $\psi_i^j(x_1)$ ,  $\psi_k^j(x_2)$ ,  $\phi_i^j(x_1)$ ,  $\phi_k^j(x_2)$  correspond to arbitrary one-dimensional wavelets and scaling functions and  $x=(x_1, x_2)$ . The  $n$ -dimensional wavelets are constructed analogously, with the exception that there will be  $2^n - 1$  distinctive  $n$ -dimensional wavelets. Note that in the case of  $n$ -dimensional tensor product wavelets, the one step of forward wavelet transform consists of the sequential application of one-dimensional wavelet transform starting from  $x_1$  direction, whereas the one step of inverse wavelet transform consists of the sequential application of one-dimensional inverse wavelet transform in reverse order starting from  $x_n$  direction. Also note that in contrast to the standard interpolating wavelets, wavelets belonging to the same family can be drastically different depending on the location of the

interface boundary. A practical form of two-dimensional discontinuous forward interpolating wavelet transform is given in Algorithm 5. An inverse transform is constructed analogously by simply reversing the order of operations analogously to the one dimensional case. As in one-dimension, multidimensional wavelets and scaling functions can be formally constructed by setting all except one wavelet coefficients to zero and then performing the inverse wavelet transform up to an arbitrary high level of resolution  $J$ . Once wavelets and scaling functions are constructed, an  $n$ -dimensional function  $f(\mathbf{x})$  can be decomposed as in Eq. (1).

#### A.3. Adaptive-wavelet based refinement

### Algorithm 6.

Reconstruction check procedure for the wavelet transform.

---

```

sample a function  $f(\mathbf{x})$  on a grid  $\mathcal{G}_{\geq}$ 
perform forward wavelet transform
for all levels  $j = 0 : 1 : J$ 
  create a mask  $\mathcal{M}$  for  $|d_{i,j}^{\mu}| \geq \epsilon$ 
end
include into mask  $\mathcal{M}$  all points at level  $j = 1$ 
for all levels  $j = J - 1 : -1 : 1$ 
  extend mask  $\mathcal{M}$  to include the minimal set
  of points for  $|d_{i,j}^{\mu}| \geq \epsilon$ 
end
  
```

---

**Algorithm 7.**

Grid adaptation procedure.  $\mathbf{u}_m^k$  is a solution vectors for all phase diagram variables.

---

```

initial guess ( $m = 0$ ):  $\mathbf{u}_k^m$  and  $\mathcal{G}_\geq^m$ 
while  $m = 0$  or  $m > 1$  and  $\mathcal{G}_\geq^m \neq \mathcal{G}_\geq^{m-1}$ 
   $m = m + 1$ 
  perform forward wavelet transform for each
  component of  $\mathbf{u}_k^m$ 
  for all levels  $j = J : -1 : 1$ 
    create a mask  $M$  for  $|d_1^{u,j}| \geq \epsilon$ 
  end
  extend the mask  $M$  with adjacent wavelets
  perform the reconstruction check procedure
  construct  $\mathcal{G}_\geq^{m+1}$ 
  if  $\mathcal{G}_\geq^{m+1} \neq \mathcal{G}_\geq^m$ 
    calculate phase diagram function at
    new points
  end if
end

```

---

As mentioned in Section 2.3, the adaptive wavelet refinement strategy is based on omitting wavelets from approximation (1) based on magnitude of their coefficients. Due to one-to-one correspondence between wavelet and grid points, the collocation point should be omitted from the computational grid if the associated wavelet is omitted from the approximation (1). Removal of collocation points in this manner presents a potential problem. Since coefficient information about  $f_\geq(\mathbf{x})$  at all locations in space is no longer available, the reconstruction of this function from the available coefficient information may not be possible. This can be easily overcome as long as one requires that all grid points required for the recursive computation of the wavelet coefficients  $d_1^{u,j}$  present in the approximation  $f_\geq(\mathbf{x})$  are available. This is achieved by the additional procedure, called the *perfect reconstruction check*, which ensures that all grid points required for the recursive computation of the wavelet coefficients  $d_1^{u,j}$  (hereafter referred as *minimal set* of grid points), present in the approximation  $f_\geq$  are available. For details of the perfect reconstruction check procedure and its implementation in multiple dimensions, we refer to [22]. The pseudocode for the perfect reconstruction check procedure is shown in Algorithm 6. When constructing the phase diagram, the calculation for each point

in  $P$ – $T$  space can be expensive by itself. Thus, minimizing the number of evaluations is essential and a strategy for progressive grid refinement should be developed. The calculations should start on a coarse grid in  $P$ – $T$  space. Additional grid points are progressively added with increasing resolutions into the regions dictated by the phase diagram. The addition of grid points is based on an analysis of wavelet coefficients: points are added at locations where wavelet coefficients are or are predicted to be significant. In other words, the computational grid should include “adjacent” points at the finer scale in the immediate neighborhood of wavelets for which the magnitude of their coefficients is greater than an a priori prescribed threshold. The adaptive gridding procedure is illustrated in Algorithm 7.

**References**

- [1] D.L. Turcotte, G. Schubert, *Geodynamics: Application of Continuum Physics to Geological Problems*, Wiley, New York, 1982.
- [2] H. Schmeling, R. Monz, D.C. Rubie, The influence of olivine metastability on the dynamics of subduction, *Earth Planet. Sci. Lett.* 165 (1998) 55–66.
- [3] C. Guinchi, Y. Ricard, High-pressure/low-temperature metamorphism and the dynamic of an accretionary wedge, *Geophys. J. Int.* 136 (1999) 620–628.
- [4] J. van Hunen, A.P. van den Berg, N.J. Vlaar, A thermo-mechanical model of horizontal subduction below an overriding plate, *Earth Planet. Sci. Lett.* 182 (2000) 157–169.
- [5] R. Bousquet, B. Goe, P. Henry, X.L. Pichon, C. Chopin, Kinematic, thermal and petrological model of the central Alps: Lepontine metamorphism in the uppercrust and eclogitisation of the lower crust, *Tectonophysics* 273 (1997) 105–127.
- [6] D. Bittner, H. Schmeling, Numerical modeling of melting processes and induced diapirism in the lower crust, *Geophys. J. Inter.* 123 (1995) 59–70.
- [7] T.V. Gerya, B. Stoeckert, A.L. Perchuk, Exhumation of high-pressure metamorphic rocks in a subduction channel—a numerical simulation, *Tectonics* 6 (21) (2002) 1–19.
- [8] T.V. Gerya, D.A. Yuen, Rayleigh–Taylor instabilities from hydration and melting propel ‘cold plumes’ at subduction zones, *Earth Planet. Sci. Lett.* 212 (2003) 47–62.
- [9] I.K. Karpov, A.I. Kiselev, F.A. Letnikov, *Computer Modeling of Natural Mineral Formation*, Nedra Press, Moscow, 1976, in Russian.
- [10] R.G. Berman, Internally-consistent thermodynamic data for minerals in the system  $\text{Na}_2\text{O}$ – $\text{K}_2\text{O}$ – $\text{CaO}$ – $\text{MgO}$ – $\text{FeO}$ – $\text{Fe}_2\text{O}_3$ – $\text{Al}_2\text{O}_3$ – $\text{SiO}_2$ – $\text{TiO}_2$ – $\text{H}_2\text{O}$ – $\text{CO}_2$ , *J. Petrol.* 29 (1988) 445–522.
- [11] T.J.B. Holland, R. Powell, An enlarged and internally con-

- sistent dataset with uncertainties and correlations: the system  $K_2O-Na_2O-CaO-MgO-MnO-FeO-Fe_2O_3-Al_2O_3-TiO_2-SiO_2-C-H_2-O_2$ , *J. Metamorph. Geol.* 8 (1990) 89–124.
- [12] T.J.B. Holland, R. Powell, Internally consistent thermodynamic data set for phases of petrological interest, *J. Metamorph. Geol.* 16 (1998) 309–344.
- [13] J.A.D. Connolly, D.M. Kerrick, An algorithm and computer program for calculating composition phase diagrams, *CALPHAD* 11 (1987) 1–55.
- [14] C. de Capitani, T.H. Brown, The computation of chemical equilibrium in complex systems containing non-ideal solid solutions, *Geochim. Cosmochim. Acta* 51 (1987) 2639–2652.
- [15] S.V. Sobolev, A.Y. Babeyko, Modeling of mineralogical composition, density and elastic wave velocities in anhydrous magmatic rocks, *Surv. Geophys.* 15 (1994) 515–544.
- [16] T.V. Gerya, W.V. Maresch, A.P. Willner, D.D. Van Reenen, C.A. Smit, Inherent gravitational instability of thickened continental crust with regionally developed low- to medium-pressure granulite facies metamorphism, *Earth Planet. Sci. Lett.* 190 (2001) 221–235.
- [17] T.V. Gerya, L.L. Perchuk, W.V. Maresch, A.P. Willner, D.D. Van Reenen, C.A. Smit, Thermal regime and gravitational instability of multi-layered continental crust: implications for the buoyant exhumation of high-grade metamorphic rocks, *Eur. J. Mineral.* 14 (4) (2002) 687–699.
- [18] D.M. Kerrick, J.A.D. Connolly, Metamorphic devolatilization of subducted oceanic metabasalts: implications for seismicity, arc magmatism and volatile recycling, *Earth Planet. Sci. Lett.* 189 (2001) 19–29.
- [19] J.A.D. Connolly, K. Petrini, An automated strategy for calculation of phase diagram sections and retrieval of rock properties as a function of physical conditions, *J. Metamorph. Geol.* 20 (2002) 697–708.
- [20] G. Xu, J.F. Brennecke, M.A. Stadtherr, Reliable computation of phase stability and equilibrium from the Saft equation of state, *Ind. Eng. Chem. Res.* 41 (5) (2002) 938–952.
- [21] O.V. Vasilyev, N.K.R. Kevlahan, An adaptive wavelet collocation method for fluid structure interaction, *Bull. Am. Phys. Soc.* 47 (10) (2002) 186.
- [22] O.V. Vasilyev, Solving multi-dimensional evolution problems with localized structures using second generation wavelets, *Int. J. Comp. Fluid Dyn. (Spec. Iss. High-Resolut. Methods Comput. Fluid Dyn.)* 17 (2) (1999) 151–168.
- [23] O.V. Vasilyev, N.K.-R. Kevlahan, Hybrid wavelet collocation—Brinkman penalization method for complex geometry flows, *Int. J. Numer. Methods Fluids* 40 (2002) 531–538.
- [24] R. Powell, T.J.B. Holland, Relating formulations of the thermodynamics of mineral solid solutions: activity modeling of pyroxenes, amphiboles, and micas, *Am. Mineral.* 84 (1999) 1–14.
- [25] J. Dale, T.J.B. Holland, R. Powell, Hornblende–garnet–plagioclase thermobarometry: a natural assemblage calibration of the thermodynamics of hornblende, *Contrib. Mineral. Petrol.* 140 (2000) 353–362.
- [26] M.S. Ghiorso, R.O. Sack, Chemical mass transfer in magmatic processes: IV. A revised and internally consistent thermodynamic model for the interpolation and extrapolation of liquid–solid equilibria in magmatic systems at elevated temperatures and pressures, *Contrib. Mineral. Petrol.* 119 (1995) 197–212.
- [27] P.D. Asimow, M.S. Ghiorso, Algorithmic modifications extending MELTS to calculate subsolidus phase relations, *Am. Mineral.* 83 (1998) 1127–1131.
- [28] D.L. Donoho, Interpolating wavelet transforms, *Tech. Rep.* 408, Department of Statistics, Stanford University (1992).
- [29] A. Harten, Adaptive multiresolution schemes for shock computations, *J. Comput. Phys.* 115 (1994) 319–338.
- [30] W. Sweldens, The lifting scheme: a custom-design construction of biorthogonal wavelets, *Appl. Comput. Harmon. Anal.* 3 (2) (1996) 186–200.
- [31] W. Sweldens, The lifting scheme: a construction of second generation wavelets, *SIAM J. Math. Anal.* 29 (2) (1998) 511–546.
- [32] W. Sweldens, P. Schröder, Building your own wavelets at home, *Wavelets in Computer Graphics*, ACM SIGGRAPH Course notes, 1996, pp. 15–87.
- [33] B.W.D. Yardley, An introduction to metamorphic petrology, *Earth Sci. Ser.* 98 (1989) 248.
- [34] O.V. Vasilyev, N.K.-R. Kevlahan, An adaptive multilevel wavelet collocation method for elliptic problems, *J. Comp. Phys.* (2004) (submitted for publication).
- [35] D. Donoho, Unconditional bases are optimal bases for data compression and for statistical estimation, *Appl. Comput. Harmon. Anal.* 1 (1993) 100–115.
- [36] T.V. Gerya, L.L. Perchuk, W.V. Maresch, A.P. Willner, Inherent gravitational instability of hot continental crust: implication for doming and diapirism in granulite facies terrains, *Gneiss Domes and Orogeny*, GSA book, 2004, in press.
- [37] T.V. Gerya, L.L. Perchuk, D.D. Van Reenen, C.A. Smit, Two-dimensional numerical modeling of pressure–temperature–time paths for the exhumation of some granulite facies terrains in the Precambrian, *J. Geodyn.* 29 (2000) 17–35.
- [38] T.V. Gerya, D.A. Yuen, Characteristics-based marker-in-cell method with conservative finite-differences schemes for modeling geological flows with strongly variable transport properties, *Phys. Earth Planet. Inter.* 140 (2003) 295–320.
- [39] S.A. Barboza, G.W. Bergantz, Melt productivity and rheology: complementary influences on the progress of melting, *Numer. Heat Transf., Part A* 31 (1997) 375–392.
- [40] T.V. Gerya, R. Uken, J. Reinhardt, M.K. Watkeys, W.V. Maresch, B.M. Clarke, Cold fingers in a hot magma: numerical modeling of diapirs in the Bushveld Complex, South Africa, *Geology* 31 (9) (2003) 753–756.
- [41] T.V. Gerya, D.A. Yuen, E.O.D. Sevre, Dynamical causes for incipient magma chambers above slabs, *Geology* 32 (2004) 89–92.
- [42] Z.A. Garbow, N.R. Olson, D.A. Yuen, J.M. Boggs, Interactive web-based map: applications to large data sets in the geosciences, *Electron. Geosci.* 6 (2001).
- [43] A. Ten, D. Yuen, Y.Y. Podladchikov, Visualization and analysis of mixing dynamical properties in convecting systems with different rheologies, *Electron. Geosci.* 4 (1999).

- [44] C.W. Passchier, R.A. Trow, *Microtectonics*, Springer-Verlag, Berlin, 1996.
- [45] A. Dimanov, G. Dresen, R. Wirth, High-temperature creep of partially molten plagioclase aggregates, *J. Geophys. Res. Solid Earth* 103 (1998) 9651–9664.
- [46] A. Dimanov, R. Wirth, G. Dresen, The effect of melt distribution on the rheology of plagioclase rocks, *Tectonophysics* 328 (2000) 307–327.
- [47] G. Ranalli, *Rheology of the Earth*, 2nd edition, Chapman & Hall, London, 1995.
- [48] B. Evans, D.L. Kohlstedt, Rheology of rocks, in: T. Ahrens (Ed.), *Rock Physics and Phase Relations, A Handbook of Physical Constants*, American Geophysical Union, Washington, DC, 1995, pp. 148–165.
- [49] J. Renner, B. Stackhert, A. Zerbian, K. Roller, F. Rummel, An experimental study into the rheology of synthetic polycrystalline coesite aggregates, *J. Geophys. Res.* 106 (2001) 19411–19429.
- [50] C. Denison, W.D. Carlson, R.A. Ketcham, Three-dimensional quantitative textural analysis of metamorphic rocks using high-resolution computed X-ray tomography: 1. Methods and techniques, *J. Metamorph. Geol.* 15 (1) (1997) 29–44.
- [51] C. Denison, W.D. Carlson, Three-dimensional quantitative textural analysis of metamorphic rocks using high-resolution computed X-ray tomography: 2. Application to natural samples, *J. Metamorph. Geol.* 15 (1) (1997) 45–57.
- [52] T. Rowe, W.D. Carlson, R.A. Ketcham, C. Denison, J. Kappelman, High-resolution computed tomography—a breakthrough technology for earth scientists, *Geotimes* 42 (9) (1997) 23–27.
- [53] D.L. Kohlstedt, B.K. Holtzman, Shearing melt out of the mantle, *Geochim. Cosmochim. Acta* 66 (15A) (2002) A410–A411.
- [54] M.A. Brown, M. Brown, W.D. Carlson, C. Denison, Topology of syntectonic melt-flow networks in the deep crust: inferences from three-dimensional images of leucosome geometry in migmatites, *Am. Mineral.* 84 (1999) 1793–1818.
- [55] G. Erlebacher, D.A. Yuen, F. Dubuffet, Current trends and demands in visualization in the geosciences, *Electron. Geosci.* 4 (1999).
- [56] V.S. Solomatov, R. El-Khozondar, V. Tikare, Grain size in the lower mantle: constraints from numerical modelling of grain growth in two-phase systems, *Phys. Earth Planet. Inter.* 129 (2002) 265–282.
- [57] K. Mibe, T. Fujii, A. Yasuda, Control of the location of the volcanic front in island arcs by aqueous fluid connectivity in the mantle wedge, *Nature* 401 (1999) 259–292.
- [58] O.V. Vasilyev, C. Bowman, Second generation wavelet collocation method for the solution of partial differential equations, *J. Comp. Phys.* 165 (2000) 660–693.
- [59] G. Deslauriers, S. Dubic, Symmetric iterative interpolation process, *Constr. Approx.* 5 (1989) 49–68.
- [60] P. Schröder, S. Dubic, Spherical wavelets: texture processing, in: P. Hanrahan, W. Purgather (Eds.), *Rendering Techniques '95*, Springer Verlag, Wien, 1995, pp. 252–263.